Dynamic range and sensitivity comparison of optical CCDs

Contact: dean.rusby@stfc.ac.uk

D. R. Rusby and P.McKenna
Department of Physics,SUPA,
University of Strathclyde,
Glasgow, G1 1XQ, Scotland, UK

D. Neely
Central Laser Facility, STFC,
Rutherford Appleton Laboratory,
Oxon OX11 0QX, United Kingdom

1 Introduction

The CLF own and use a variety of high dynamic range CCD cameras that are used for a variety of measurements on many of the experiments performed at the facility. The performance and characteristics of these cameras are of utmost importance when choosing which camera to use in any particular circumstance. Therefore, a calibration to determine the dynamic range and threshold sensitivity of the cameras has been conducted.

The cameras tested were the Starlight Express 16bit CCD camera, the Andor Neo which has a 16bit CMOS sensor with the capability of dual amplification, the Andor Ixon which has a 16bit Electron Multiplying CCD (EMCCD), a 16bit EMCCD Raptor Kite and a 14bit Allied Vision Technology Stingray camera. Basic information about each camera can be found in table 1.

2 Linearity/dynamic range test

A pulsed LED source with an operational wavelength of 565nm was focused onto the CCD chip with a 50mm diameter, 150mm focal length lens. The Raptor KITE was added at a later date using a 50mm diameter, 100mm focal length lens, with the data being normalised by comparing an Andor Ixon with the new set-up to the old set-up. The rise time of the LED was measured and was found to be 1ms. All cameras were externally triggered using the same SRS pulse genrator unit. For all the tests, the camera had an exposure time of 200ms, with the LED flashing for 50ms to ensure that the LED pulse fell well within the exposure time window of the cameras. To further ensure this, the LED pulses delay was altered to observe whether the intensity on the camera changed. Seeing no obvious change confirmed the pulse fell within the acquisition time.

Eight background images (just using the light shield without the LED) and dark current images (blocking the sensitive area entirely to prevent any light entering) were taken for each camera. The average counts and standard deviation of the background and dark current were measured. For each of the cameras used the dark current and background images show very little difference, with very few counts between the mean values of the two. This allows for simple background subtraction. An average of all the eight background images were taken yielding an average background image. The standard deviation of this image is reduced from the previous background standard deviation by a factor of $\sqrt{8}$, therefore providing a better background image to subtract from the exposed images.

Each camera was exposed to the LED pulse through varying neutral density filters, which altered in iterations of 0.5 O.D till the LED was no longer visible. All the cameras were tested with no gain, except for the Neo which requires a gain setting to be chosen, for which the setting 4+1 was used. After the images were obtained and background subtracted, an area of the image with uniform saturation at 0 ND was chosen where the mean and standard deviation were measured.

Table 1: Information about the cameras used in this study

Camera	Sensor Type	Active pixels (W x H)	Sensor Size (mm)	Pixel Size (μm)	Model Number	Body Size (cm)	Lens Mounting	Cooling
Andor - Neo	CMOS	2560 x 2160	16.6 x 14.0	6.5	DC-152Q-C00-F1	14.3 x12 x 15.9	C-mount	cooling to -40C
Starlight Express	CCD	4032 x 2688	36.3 x 24.2	9	SXVR H35	9.8 x 10 x 7.2	K/nikon mount	Achievable -10 degrees
AVT - Stingray	CCD	656 x 492	6.49 x 4.87	9.9	F-033B/C	7 x 3 x 4.4	C-mount	None
Andor - Ixon	EMCCD	1024 x 1024	13.3 x 13.3	13	DU-888-C00-#BV	17.4 x 14.8 x 13.9	C-mount	cooling to -100C (including water cooling)
Raptor - Kite	EMCCD	658 x 492	6.58 x 4.96	10		6.8 x 6.1 x 9.8	C-mount	-20C with ambient air @ +20C

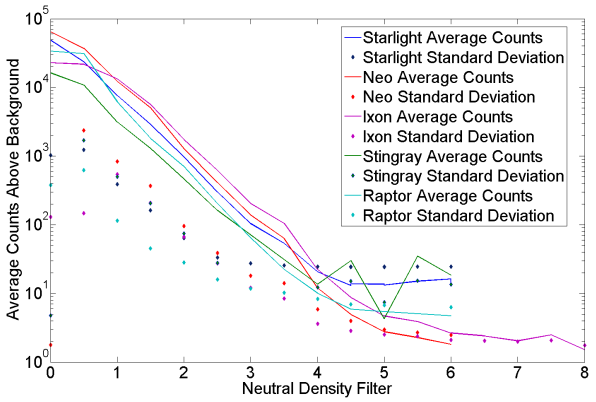

Figure 1: Average counts and standard deviation of LED incident onto the 4 CLF cameras.

This was repeated in the same position for all the images on that particular camera. The standard deviation and the average counts were plotted on the same graph, show in figure 1.

All the cameras appear to have similar linear responses between 1 and 3.5 ND. The Stingray is clearly different as it is a 14bit compared to the 3 other 16bit cameras, but the linearity is comparable. At ND 4 and above the Starlight has higher signal to noise ratio than any of the other cameras tested. This being the case, the Starlight-Express is not recommended at low light levels. The Raptor-Kite has approximately twice the sensitivity at low levels compared to the Starlight-Express. Interestingly, with no gain settings, the Ixon image 'bleeds' at 22000, meaning no data can be obtained above this value. Due to this, the Neo appears to have the largest dynamic range. It is clear however that the Andor Ixon, when comparing the average counts to the standard deviation, has the best response at low light levels. The Ixon is capable of further amplification to achieve even better signal to noise ratios at low light levels. The amplification comes in the form of 2 settings, the traditional gain setting and the electron multiplying gain setting. The gain settings used are, no gain (same as before), traditional gain of 5 then additionally an EM gain of 30 and 100.

Figure 2 shows the measured signal and standard deviation of different gain settings on the Ixon using the same method as before. The gain settings provide extra sensitivity at the very lowest light levels, which is demonstrated by the signal to noise ratio improving considerably, however the dynamic range appears reduced. Further proof can be seen when comparing the same filtering across the different gain setting, shown in figure 3. The image of the LED on the right can easily be resolved and measured, whereas the image on the left cannot be seen.

Table 3: Maximum and minimum values for the region of linearity for each camera.

Camera	Minimum signal above noise/region of linearity	Maximum signal (approximate)
Andor - Neo	5	65000
Starlight Express	2.6	21000
AVT - Stingray	30	40000
Andor - Ixon	13	10000
Raptor - Kite	10	30000

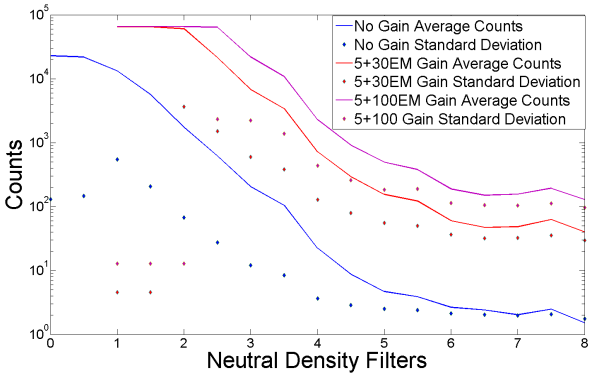

Figure 2: Average counts and standard deviation of LED incident the Andor Ixon using different gain settings.

3 Absolute Sensitivity Measurements

Each camera will have its own sensitivity to incident light, that being the amount of energy required to

Table 2: Sensitivities of the cameras using a 0.7mW, 532nm diode laser

Camera	Ixon			Neo		Starlight	Stringray		Raptor KITE
Int (s)	1	1	1	1	5	5	2	5	0.001
Gain	none	EM 20	EM 50	4+1	4+1	none	none	none	none
Photons per count	4.70	1.13	0.49	1.10	1.14	3.05	454.56	515.67	5.19
Energy per count(eV)	10.97	2.63	0.92	2.57	2.65	7.12	1060.09	1202.63	12.09

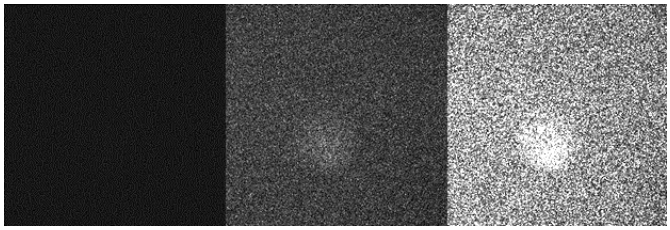

Figure 3: Images of the LED using the Andor Ixon at different gain settings. The images are all taken using the ND6 filter. From left to the right, no gain, *5+*30EM and *5+*100EM. All 3 images share the same grey-scale setting.

register on the cameras chip as a count. To measure this amount of energy, a 0.7mW green (532nm) diode laser was directed onto the chip of each camera after 7.3ND of attenuation. Knowing the wavelength, power and the integration time the energy per count for each of the cameras has be calculated and can be found in table 2. The most sensitive camera is the Ixon with the gain turned on. The Neo has a better sensitivity than the Ixon with no gain. The Starlight has comparable sensitivity to the Ixon, however, it is clear it cannot operate at the lowest light levels where the noise is greater than the signal.

4 Conclusion and Further Work

The tests conducted show that all the cameras have a large area of linearity where the standard deviation is much below the signal. Towards the lowest light levels the Ixon is superior to the other cameras, even with no gain. Turning the gain on only enhances the ability to detect signals at the low light levels, however the dynamic range appears to be compressed slightly. However the Neo has a very large dynamic range and is also very sensitive. This is down to the dual amplifier settings. The main advantage that the Starlight possesses is that it has the largest chip of the all the cameras tested. This aids in the magnification of images. It should be noted that at low signals, the signal to noise ratio will hamper results. The Stingray has a good dynamic range considering that it is the only 14 bit camera tested. Further work can be conducted on the sensitivity scan, by checking whether the sensitivity is linear by changing the ND filters.

Gamma-ray Scintillator Spectrometer

Contact: dean.rusby@stfc.ac.uk

D. R. Rusby and P. McKenna
Department of Physics, SUPA,
University of Strathclyde,
Glasgow, Scotland, UK

D. Neely and R. Clarke
Central Laser Facility, STFC,
Rutherford Appleton Laboratory,
Oxon OX11 0QX, UK

1 Introduction

Copious amounts of hard X-rays (in the 0.1-10MeV region) are typically produced in intense laser-plasma interactions. Characterising this emission enables a greater understanding of the interaction physics, including providing insight into electron dynamics inside opaque targets.

Previous gamma/X-ray spectral measurements have been conducted using thermoluminescence dosemeters (TLDs) [1], nuclear activation [1–5] or bremsstrahlung cannons [6]. The downside to these diagnostics is processing time and sensitivity. With new high power laser systems being developed that promise high repetition, a spectrometer that can operate in real time would be desirable.

A spectrometer with low processing time and high sensitivity requires a novel method of detection and x-ray attenuation. Scintillators are materials that absorb a photon that has a high energy and emit a lower energy optical photon and are therefore ideal for X-ray detection. Scintillators also have short (sub ms) decay times which means they can be used on high repetition systems.

2 Spectrometer Development

An array of scintillators that convert the x-ray into optical light, at the same time as attenuating the x-ray, could be utilised to measure the spectrum. The scintillation light is imaged and the energy deposited in the scintillators is determined. In the bremsstrahlung cannon design, x-rays are attenuated using filtering, where some of the sensitivity is lost, whereas a scintillator array provides the advantage that the x-ray signal is attenuated by the scintillator material itself, therefore providing more sensitivity.

The two scintillator materials selected for the array were bismuth germanium oxide and BC422. Bismuth germanium oxide ($Bi_4Ge_3O_{12}$), more commonly known as BGO, is a high Z and density crystal($\rho = 7.2g/cm^3$) which has a high attenuation and also a high light output. BC422 is a plastic scintillator is, in contrast a low density material ($\rho = 1.02g/cm^3$). Both of these scintillators possess different X-ray attenuation curves [7], shown in Figure 2, particularly in the high and low energy regions where the attenuation is dependent on the Z

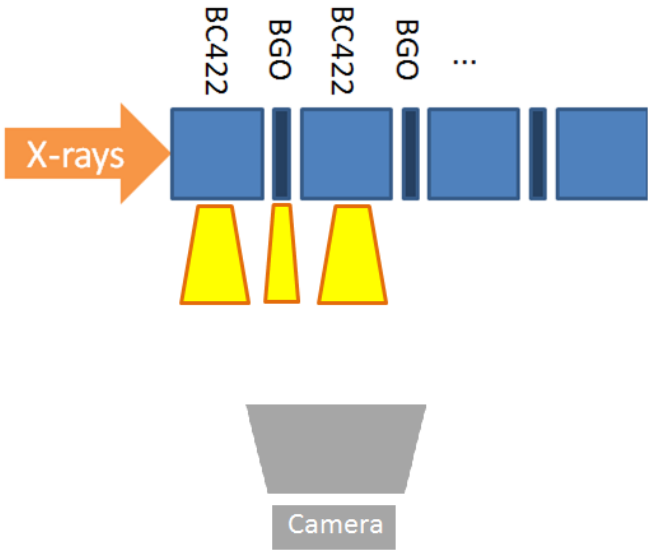

Figure 1: Schematic of the scintillator array

number of the material. BC422 has a smoother attenuation at low energies than the BGO, and is not affected as much by pair production at the highest energies. BGO has a steeper gradient than BC422 between 50KeV and 1MeV, and is much more affected by pair production at the highest energies.

Looking at different arrangement of the two materials, the spectral absorption can be found using the attenuation curves in Figure 2 and using the Beer-Lambert law for transmission, T, given by,

$$T = e^{-\sigma l N} \tag{1}$$

Where σ is the absorption cross section, l is the depth of the material and N is the density. Using equation 1 and the curves in Figure 2 it is possible to find the absorption by an array of the BGO and BC422. As discussed before, the two materials have different attenuation at the high and low energy regions, this difference can drastically change the attenuation and absorption if used correctly. Using a combination of the two materials, and matching the surface densities by adjusting the thicknesses, the absorption response of the array was optimized. The absorption response of the final configuration is shown in Figure 3.

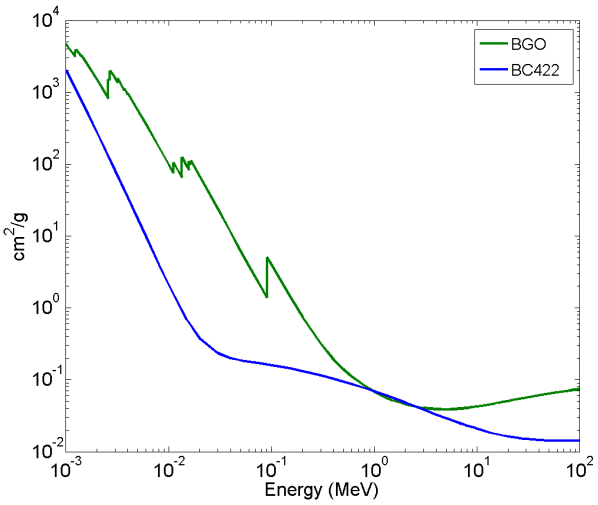

Figure 2: X-ray attenuation curves of BGO and BC422 provided by NIST

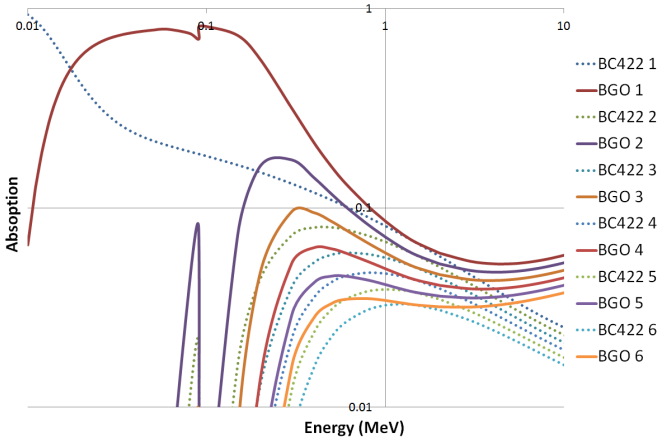

Figure 3: Absorption curves of 12mm BC422 (dotted line) and 2mm BGO (solid line).

When designing a gamma-ray spectrometer, the effects of scattering must be looked at closely. The final design was then modelled using the Monte Carlo code Geant4 to investigate the scattering effects and to verify the absorption curves produced using the NIST data. Figure 4 shows an example of a Geant4 simulation output. The energy deposited in each crystal was processed using 100,000 incident mono-energetic gamma photons, the absorption curve produced is shown in Figure 5. The curves in Figure 3 and 5 have a few differences. The BGO absorption for each crystal is very similar, however, the BC422 is very different. This can be explained when looking at the tracks in Figure 4. The thicknesses of the two crystals were adjusted so that the surface density is matched, as mentioned before, however the width and height are the same. Once an X-ray is scattered in BC422, it has less density to travel through than if it was

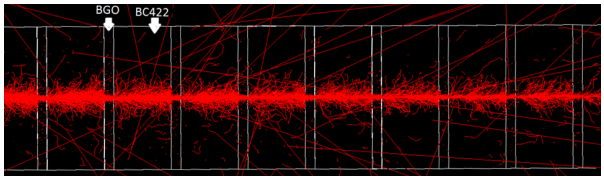

Figure 4: A typical run in Geant4 showing the excited electron tracks inside the BGO and BC422.

scattered in BGO. Inside the BGO the ionized electrons travel much shorter paths than inside the BC422, and also the only electrons that leave the array in Figure 4, leave from the BC422.

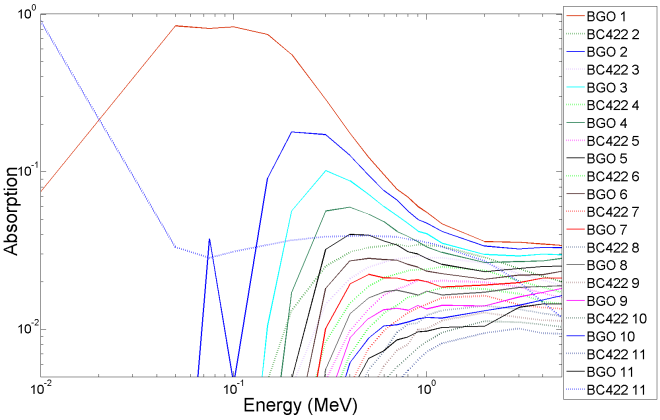

Figure 5: Response curve generated from the energy deposited in each layer using Geant4.

3 Conclusions

An array of two scintillators (BGO and BC422) was designed and optimised for the use of X-ray spectral measurements on high repetition rate, intense laser systems. The absorption curves for this array was derived from the NIST XCOM attenuation tables and simulated in Geant 4. These curves appear to show that spectral measurements can be made using the device with the configuration shown. Simulations made using Geant4 indicate that scattering does not play an important role.

References

[1] RJ Clarke, D. Neely, RD Edwards, PNM Wright, KWD Ledingham, R. Heathcote, P. McKenna, CN Danson, PA Brummitt, JL Collier, et al. Radiological characterisation of photon radiation from ultra-high-intensity laser–plasma and nuclear interactions. *Journal of Radiological Protection*, 26(3):277, 2006.

[2] PA Norreys, M. Santala, E. Clark, M. Zepf, I. Watts, FN Beg, K. Krushelnick, M. Tatarakis, AE Dangor,

X. Fang, et al. Observation of a highly directional γ-ray beam from ultrashort, ultraintense laser pulse interactions with solids. *Physics of Plasmas*, 6:2150, 1999.

[3] S.P. Hatchett, C.G. Brown, T.E. Cowan, E.A. Henry, J.S. Johnson, M.H. Key, J.A. Koch, A.B. Langdon, B.F. Lasinski, R.W. Lee, et al. Electron, photon, and ion beams from the relativistic interaction of petawatt laser pulses with solid targets. *Physics of Plasmas*, 7:2076, 2000.

[4] C Courtois, A Compant La Fontaine, O Landoas, G Lidove, V Méot, P Morel, R Nuter, E Lefebvre, A Boscheron, J Grenier, et al. Effect of plasma density scale length on the properties of bremsstrahlung x-ray sources created by picosecond laser pulses. *Physics of Plasmas*, 16:013105, 2009.

[5] C. Courtois, R. Edwards, A. Compant La Fontaine, C. Aedy, M. Barbotin, S. Bazzoli, L. Biddle, D. Brebion, JL Bourgade, D. Drew, et al. High-resolution multi-mev x-ray radiography using relativistic laser-solid interaction. *Physics of Plasmas*, 18(2):023101–023101, 2011.

[6] RHH Scott, F Pérez, MJV Streeter, EL Clark, JR Davies, HP Schlenvoigt, JJ Santos, S Hulin, KL Lancaster, F Dorchies, et al. Measuring fast electron spectra and laser absorption in relativistic laser-solid interactions using differential bremsstrahlung photon detectors. *Review of Scientific Instruments*, 84(8):083505, 2013.

[7] MJ Berger, JH Hubbell, SM Seltzer, J Chang, JS Coursey, R Sukumar, DS Zucker, and K Olsen. Xcom: Photon cross sections database. *NIST Standard reference database*, 8:87–3597, 1998.

Wavefront Sensor-less Adaptive Optics for High Powered Lasers

Contact *Lukeawalker@hotmail.co.uk*

L. Walker

Central Laser Facility
STFC Rutherford Appleton Laboratory, Chilton, Didcot, Oxon, OX11 0QX

Introduction

High Powered Lasers (HPL) require Adaptive Optics (AO) in order to correct for optical aberrations within the laser system. Such systems are typically several rooms in length and involve hundreds of individual optics; even with the highest quality of optics this allows aberrations to become cumulative. Other sources of aberration include air turbulence across the beam path and the heating of optics, all of which combine to reduce the quality of the wavefront at the output of the laser. HPLs require a high quality wavefront at the output to improve the focusability of the beam, as well as to achieve a high level of temporal pulse compression.

HPLs such as Vulcan currently use AO systems which use feedback from a Shack-Hartmann wavefront sensor to control a bimorph deformable mirror; this allows direct, closed loop control of the wavefront of a laser beam. The Shack-Hartmann sensor is positioned before the final compressor in the laser system in order to obtain the highest quality wavefront at this point. The AO systems can correct major aberrations on very short timescales (<1s), however are expensive to create – both in terms of cost of equipment and ease of setup.

An alternative to an AO that uses a wavefront sensor is that of Wavefront Sensor-less Adaptive Optics (WSAO); this does not use a wavefront sensor but rather uses a camera observing the focal spot of a beam at the required location. Using WSAO can be desirable as due to the lack of wavefront sensor it is considerably cheaper and less fragile. Another benefit is that it can be used to create focal spots other than a traditional Gaussian spot; in HPLs such as Vulcan this is sometimes required, and therefore WSAO is also arguably more appropriate in these situations. WSAO has not previously been used in the Central Laser Facility and this report aims to investigate various methods of implementing WSAO.

Theory

It is well known that the quality of an image in the focal plane of an optical system is closely dependent on the spatial quality of the wavefront, and it is on this principal that WSAO works [1]. By using methods to improve the quality of a focal spot, one can be sure that the overall spatial quality of the wavefront is also improving. To improve the quality of the focal spot, two means may be considered: the first is general search algorithms and the second is that of "intelligent" systems which can estimate the required correction from the image.

The first method – that of general searching – is already mathematically well researched and several heuristics are known for searching a system phase space to find a minimum at high speed [2]. These systems can also be highly flexible, as no prior knowledge of the function to be minimised is required, although some algorithms may be quicker if more is known about the function.

The second method – that of "intelligent" systems – is likely to be faster than the general search algorithms: an ideal system will be able to fully correct a beam in very few cycles. However such speed comes at the expense of having to model the system beforehand to provide some sort of calibration specific to the laser system.

Of these two methods, this investigation will research various general search algorithms due to their novel application to HPLs: they offer the prospect of incredible flexibility as they may be setup quickly and run without the necessity of entering any more information than the dimensions of the phase space to be searched. Systems which model the laser system are likely to take too long to produce, and therefore not justify the cost saved over traditional systems employing a wavefront sensor.

Mirrors

The Deformable Mirrors (DMs) to be used in the investigation are bimorph mirrors, created by sandwiching piezoelectric material in between a conductive "ground" plate and a layer of electrodes and applying a gold coating to the front. Applying voltages to the electrodes causes the piezoelectric material to expand laterally, causing deformation to the mirror [3].

The DM is controlled via a PCI card and driver box, and electrodes are represented as channels to the controlling software; for the software these actuators are defined by channel number, not by position on the DM itself. A voltage pattern to be applied to the DM includes a voltage for each actuator, and may therefore be represented by an array $\mathbf{V_I}$ of length N - where N is the number of actuators and the index of the array is the channel number.

The DMs may be modelled by using equation (1) which shows how the surface deformation (W) and the voltage across the piezoelectric material (V) are related [4]. If a function can be provided that relates $\mathbf{V_I}(n_{chan})$ to V(x, y) and vice versa – a lookup table would suffice – then this equation can be solved relatively simply to provide a model of the surface deformation of the mirror. In most HPL situations the geometry of the mirror is fixed, so search algorithms which make use of a model of a mirror may have increased functionality, without too much of a decrease in flexibility.

$$\nabla^4 W(x,y) + A\nabla^2 V(x,y) = 0 \qquad (1)$$

Metrics

To produce a search algorithm a function must be identified to measure the quality of the focal spot and relate this to the voltage pattern of the mirror; this is what the search algorithm will attempt to minimise. In practice this function will be an image metric that can be calculated from an image which is obtained after a certain voltage pattern $\mathbf{V_I}$ has been applied to the DM.

Various different metrics have been identified that can be measured from the image of a focal spot and that are also related to the wavefront error; of these the I^3 power metric (2) is notable, as is the "Power in the Bucket" (3) metric [5]. The "Power in the Bucket" metric may be normalised against the total energy contained within an image, resulting in a metric which is not dependent on energy stability; this metric is also desirable as there is a theoretical limit (84%) to the energy contained within the first ring of an Airy pattern. This metric,

however, relies on accurate methods to find the centroid of the beam, and is not proven to have a global maximum that is well defined within the phase space to be searched.

$$I^3 = \int_0^X \int_0^Y I(x,y)^3 \, dxdy \quad (2)$$

$$I_{\mathrm{PiB}} = \iint_A I(x,y) \, dxdy \quad (3)$$

The I^3 metric does not have a theoretical upper limit - although if enough is known about the system this can be estimated – and may not be normalised against the total energy contained within the image. Previous investigations have, however, showed that compared to the other power law metrics, I^3 takes fewest iterations to arrive at a goal and for this reason, I^3 was chosen to be the image metric that would be evaluated [5].

Search Algorithms

Once the function to be minimized has been identified, the next stage is simply that of finding the optimum method of minimising this function. A few algorithms for finding minima were investigated to find the most suitable for use in an HPL, the first of which was "Surface Fitting" and the second of which was the well-known "Nelder-Mead method" [6]. For each of these algorithms, a method that involved knowledge of each actuator position and a method which did not were investigated.

The first method to be investigated was that of "Surface Fitting"; this involved splitting the DM into groups of actuators. Initially the entire DM functions as one big group, and then the group is split into 2, then each of these in 2, etc. The algorithm then searches the phase space of the mirror by moving all the actuators in a group the same direction and at the same voltage, and moving successive groups. Once all the groups at one size of group have been optimized, the groups are split into smaller groups and the process repeated. Actuators were put into groups depending on their channel number, irrespective of their position on the mirror; for this reason, this algorithm was dubbed "Surface Fitting by Index". At each stage an area local to the current voltage of the actuators only was searched: this increased the speed at which the algorithm would run, and also attempted to address the problem of crosstalk between the actuators and hysteresis within the DM, as smaller movements were used with smaller groups [3].

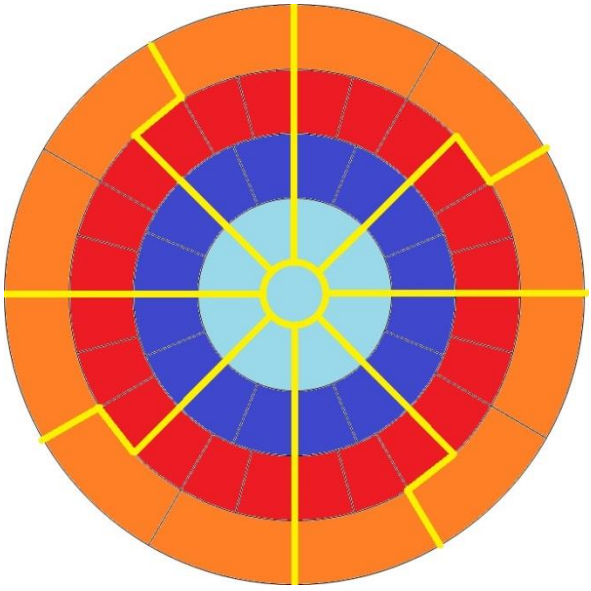

Figure 1: Grouping by Position; groups are shown in varying colours

The "Surface Fitting" algorithm was also attempted with knowledge of each actuator position; dubbed "Surface Fitting by Position", in this algorithm groups of actuators were decided based on the geometry of the mirror, rather than the channel number. The groups can be seen in figure 1: initially the entire mirror was one group, then the mirror was split into two rings (blues and reddy-orange), then these were split into individual rings (individual colours), then each of these groups were split along the yellow lines, so there were then 33 groups and finally individual actuators were moved.

The other algorithm that was investigated was the well-known Nelder-Mead method, otherwise known as the downhill simplex method. This method involves generating N+1 (where N is the number of actuators) voltage patterns to test within the phase space of the DM; each voltage pattern is an array of N voltages which can be applied to the actuators on the DM, for this reason, this algorithm was dubbed the "Simplex by Index" algorithm. For each voltage pattern the result of the image metric is recorded and stored in a separate array. Once all the results are known, they are assembled in order of most desirable to least desirable, and then the voltage pattern with the least desirable result is reflected through the centre of gravity of the other voltage patterns. Once this has been done the point is re-evaluated, and the algorithm starts a new iteration by reordering the results and finding the new least desirable pattern. Depending on the result of changing the least desirable pattern, a number of different actions can be taken, including drawing all the points closer to the current most desirable pattern by a factor of two and re-evaluating all of them – known as "contracting" the simplex [6].

This algorithm was also tried with an alternative: the mirror was modelled using (1) to find the appropriate voltage pattern to apply to create a normalised Zernike polynomial on the surface of the mirror. Knowing this, the simplex algorithm could also be tried with each vertex representing a set of Zernike coefficients, rather than an actual voltage pattern. Dubbed the "Simplex by Zernike" algorithm, this would then have the benefit of its speed not being dependent on the number of actuators on a DM.

Each of these algorithms has benefits: the non-positional dependent algorithms will be highly flexible as only knowledge of the number of actuators is required, whereas those that are pre-programmed are likely to be faster. The quality of result of the surface fitting algorithms and the non-positional dependent simplex algorithm are predicted to be equivalent, whereas that of the Zernike-modelling algorithm is likely to be lower as individual actuators are not considered. An advantage of the surface fitting algorithms is that they are predictable in terms of speed, whereas the simplex algorithms rely on parameters that may change during the run, so the speed cannot be estimated in advance.

Experiment

The algorithms were all tested in a temperature controlled laboratory with the setup shown below (figure 2). An IR laser was passed through a spatial filter, reflected off various mirrors (including a gold coated DM with 61 actuators (figure 1)) and focused down onto a UI-1540SE CCD camera. The mirror was relaxed to a reference starting point and then the algorithm was run in an attempt to allow the mirror to correct for its own inherent aberrations.

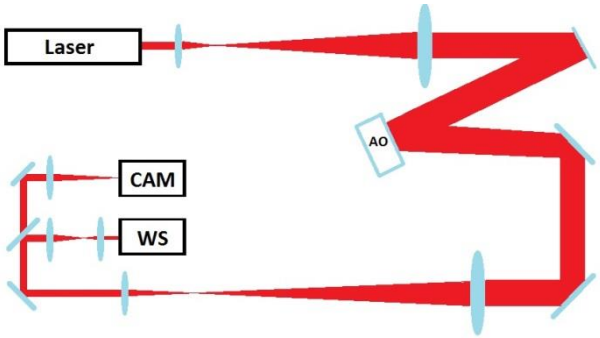

Figure 2: WSAO Experimental Layout

The test cycle – relaxation followed by a search for the best far field – was conducted 100 times for each search algorithm. Images were captured at relevant points within the algorithm, and the time taken to reach this point since the beginning of the search was recorded. Once these images had been compounded, they were analysed to retrieve the value of the image intensity squared metric (4); this metric is proven to relate to the quality of a focal spot, but was not chosen for minimisation due to previous investigations [5].

$$I^2 = \int_0^X \int_0^Y I(x,y)^2 \, dxdy \qquad (4)$$

Results

Initially the results that were compiled were drawn onto a single graph for a direct comparison. In figure 3 the graphs of I^2 metric against time can be seen – this was calculated as the average result of the I^2 metric over 100 iterations of the algorithm; error bars equal to the standard deviation of the results have also been included. It can be seen that there is a great variety of achieved focal spot quality and time taken.

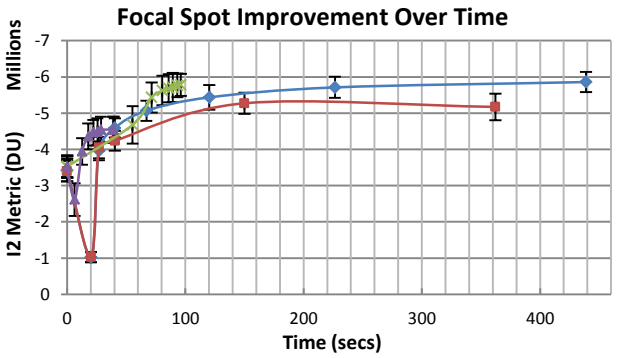

Figure 3: A comparison of various search algorithms: "Simplex by Zernike" (Purple Triangles), "Simplex by Index" (Green Crosses), "Surface Fitting by Index" (Blue Diamonds) and "Surface Fitting by Position" (Red Squares)

When tested, the "Surface Fitting by Index" algorithm would run reliably in 440 seconds and finish with a much higher quality focal spot than the initial (see figure 4). In figure 3, this algorithm is represented by blue diamonds; it can be seen that despite the time taken by the algorithm, the algorithm is approaching the minimum of -5.9E-06 DU by 230 seconds. This algorithm reached the lowest average minimum.

The next test was of the "Surface Fitting by Position" algorithm – represented by red squares in figure 3 – which would reliably run in 360 seconds. There was a minor difference in the quality of the focal spot produced by this algorithm from that of the "Surface Fitting by Index" algorithm, this algorithm manages a final focal spot of -5.2E6 DU. It can be seen that for this algorithm the minimum of -5.3E6 DU is reached at approximately 150 seconds, and further action only degrades the spot.

The "Simplex by Index" method was also tested – represented by green crosses - and it was seen that the final focal spot quality was very similar to the other two algorithms, finishing at -5.8E06 DU. However this quality was achieved at a much greater speed, the algorithm finished running after 96 seconds on average.

Finally the "Simplex by Zernike" method was tested (Seen in figure 3 represented by purple triangles); this method produced a much lower quality spot than the other algorithms, reaching a minimum of only -4.5E06 DU. This method reached the maximum in only 18 seconds however, making it the fastest algorithm. In figure 4, it can be seen that the final focal spot is dimmer than the others, and that more energy is distributed in the Airy rings.

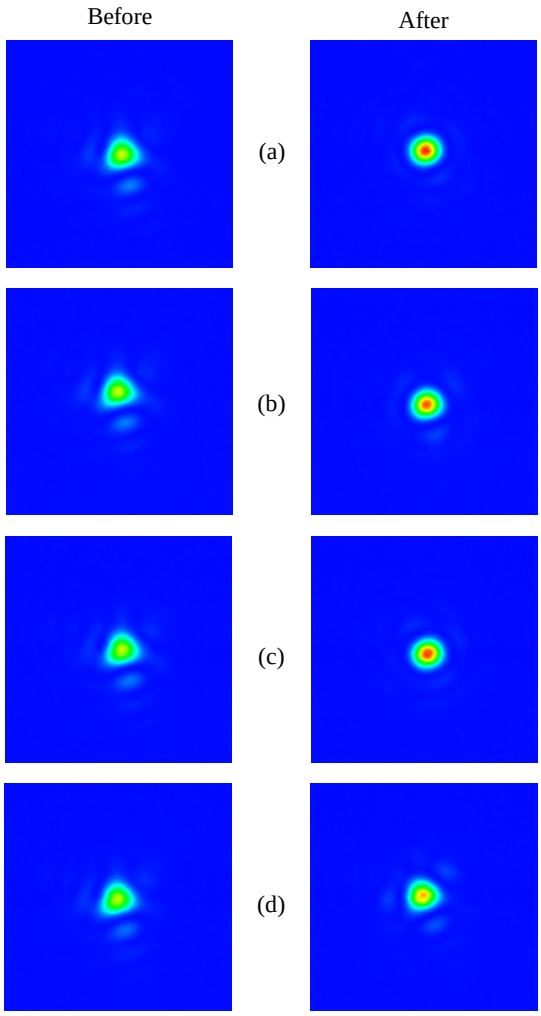

Figure 4: Focal spot before (left) and after (right) algorithms: (a) Surface Fitting by Index, (b) Surface Fitting by Position, (c) Simplex by Index, (d) Simplex by Zernike

Conclusions

In terms of speed it is clear that the "Simplex by Zernike" algorithm is the quickest, reaching the minimum at least 5 times faster than any other algorithm. This is due to the fact that this algorithm has fewest variables to search, which allows a considerably quicker convergence. Despite the lower quality of result, this algorithm may be suitable for use in an HPL situation if the time between shots is short.

In terms of quality, it can be seen that the two "Surface Fitting" algorithms and the "Simplex by Index" algorithm produce a focal spot quality which is indistinguishable to the eye. The lower quality of the "Simplex by Zernike" algorithm matched that which was predicted due to the lack of control over individual actuators; however future investigations could follow the effect of an individual actuator optimisation algorithm following a run of the "Simplex by Zernike" algorithm.

Despite the lower quality of the "Simplex by Zernike" algorithm, the first Airy rings can be seen on all the final focal spots, which shows that WSAO is capable of improving the quality of the wavefront to close to the theoretical limit of the system.

The best algorithm in terms of compromise between quality of result and time taken is clearly the "Simplex by Index" method, and this is likely to be the method which is taken forward for future testing, although further investigation into other suitable WSAO algorithms will be attempted. Further investigation may also be undertaken to find an algorithm capable of maintaining a high quality of wavefront continuously to maintain a high quality focal spot over long periods of time.

Acknowledgements

Thanks to Chris Hooker and Bryn Parry for their aid in the experimental setup.

References

1. Tyson, R, 2010. *Principles of Adaptive Optics.* 3rd Ed. CRC Press.
2. Press W., Flannery B., Teukolsky S., Vetterling W., 1992. *Numerical Recipes in C: The Art of Scientific Computing*. 2nd Ed. Cambridge University Press.
3. M. J. Shaw, C. Hookerm C. Reason, T Kanèko, *Development of an Adaptive Optic System for Laser Phasefront Control*. Central Laser Facility Annual Report 1996/1997, Pgs 213 - 215
4. J. Collier, C. Hooker, *A predictive analysis of the performance of a bimorph mirror,* Central Laser Facility, Annual Report 2000/2001, pgs 177-180.
5. Murray L. P., Dainty J. C., Daly L., 2005. *Wavefront correction through image sharpness maximisation*. National University of Ireland.
6. Nelder J. A., Mead R., 1965. *A Simplex Method for Function Minimization.* The Computer Journal Vol 7, No. 4. Pp. 308-313.